

Numerical efficiency of explicit time integrators for phase-field models

Marco Seiz^{a,c}, Tomohiro Takaki^{a,b,c}

^a*Faculty of Mechanical Engineering, Kyoto Institute of Technology, Matsugasaki, Sakyō-ku, 606-8585, Kyoto, Japan*

^b*High-Performance Simulation Research Center, Kyoto Institute of Technology, Matsugasaki, Sakyō-ku, 606-8585, Kyoto, Japan*

^c*Corresponding authors takaki@kit.ac.jp*

Abstract

Phase-field simulations are a practical but also expensive tool to calculate microstructural evolution. This work aims to compare explicit time integrators for a broad class of phase-field models involving coupling between the phase-field and concentration. Particular integrators are adapted to constraints on the phase-field as well as storage scheme implications. Reproducible benchmarks are defined with a focus on having exact sharp interface solutions, allowing for identification of dominant error terms. Speedups of 4 to 114 over the classic forward Euler integrator are achievable while still using a fully explicit scheme without appreciable accuracy loss. Application examples include final stage sintering with pores slowing down grain growth as they move and merge over time.

Keywords: phase-field, time integration, grain growth, final stage sintering

1. Introduction

The phase-field method is applied in many contexts to determine how microstructures evolve, with goals such as optimizing a process or explain its mechanisms. A phase-field model typically consists of a specified free energy, which is minimized by an appropriate gradient flow, resulting in a set of partial differential equations (PDEs) for the spatiotemporal evolution. Since these PDEs are typically not analytically solvable, numerical solutions are required and thus discretizations in space and time. Hence the efficiency of these discretizations becomes an interesting topic to study.

For the spatial discretization a number of “soft” factors play a major role, such as whether an employed framework allows for adaptive mesh refinement, whether it is parallelized (efficiently), whether the order of spatial approximation can be changed easily and many more. In contrast, temporal discretization is often done with the method of lines on top of a spatial semi-discretization. Assuming the employed time integrator covers the relevant parts of the stability domain, the efficiency can be investigated somewhat in isolation from the specific spatial discretization and so may be transferable between different spatial discretizations. Furthermore, if explicit schemes are employed, then no additional “soft” factors such as e.g. the ease of constructing appropriate

preconditioners enters the question, making the decision among such schemes particularly easy. Hence the goal of the present paper is to investigate the time integration efficiency of various explicit integrators for phase-field applications.

We note that the time evolution of different processes in the microstructure may span several orders of magnitude, making the simple forward Euler scheme often quite inefficient. This may simply stem different timescales of the equations, but may also couple into externally given control of a field parameter. Examples of the latter include e.g. the thermal control during solidification and sintering, where process times may be on the order of minutes to hours depending on the cooling/heating rate. Resolving the microstructure with relevant diffusivities then often puts the stable time step on the order of microseconds or less, making full-process simulations expensive to unfeasible. Another consideration, especially for sintering, is that the process speed depends on the grain size G as a power function. For example, if densification occurs via grain boundary diffusion the densification speed can scale as G^{-4} [1]. Hence increasing the scale of simulation from e.g. a grid spacing of 1 to 10 makes this process 10^4 times slower, but a forward Euler scheme gains only a factor of 10^2 in its stable timestep, which means simulating to equivalent density takes 100 times as long! As the physical process occurs that much slower, unconditionally stable integrators can easily increase their time step substantially with little precision loss.

For the present paper, the focus will be on models with so-called obstacle potentials, which take on finite energy values in part of the domain, but infinite outside of it. This causes the evolution of the phase-field to be trivial outside of a narrow-band called the interface, with the remaining part of the domain being called bulk. Identification of the narrow-band can then be used to speed up simulations by not requiring the calculation of updates outside of it. The time integration needs to account for the infinite potential, which is often done using a projection approach[2, 3].

Although there is a large literature of integrators specifically crafted for the Cahn-Hilliard equation[4–10] and many more, where the fourth-order nature makes the stiffness much more acute, a thorough efficiency comparison between them is more rare [5, 6, 9, 10]; the focus is generally on assuring energy stability, i.e. that the monotonic decrease of energy predicted by the continuous problem also holds in the discrete case. This applies even more so for the Allen-Cahn equation[6, 7, 9], with no comparative efficiency investigations being found in the literature at all for obstacle potentials with explicit integrators. Hence this work intends to start to fill this gap by answering the following set of questions:

- Does the energy stability of a time integrator play a significant role for convergence to the sharp interface limit?
- How coarse can integration tolerances be taken before they dominate spatial and interface width errors?
- How much quicker can explicit time integration become over the forward Euler integration for obstacle potentials?

To answer these questions, benchmark geometries with analytical solutions are defined, which allow for a more appropriate performance comparison than using a reference solution. However, these do suffer from usually being restricted

to simpler geometry and parameter combinations. Hence a final geometry, grain growth with and without mobile or immobile particles, is also considered as a more complex geometry spanning several orders of magnitudes in its parameters.

2. Model

A phase-field model using an obstacle potential will be employed within the present work, with coupling to mass diffusion realized via a Kim-Kim-Suzuki approach[11]. The independent variables are the phase-field $\phi(x, t)$ with N entries and the concentration $c(x, t)$ with $K = 1$ independent entries whose arguments will be dropped for brevity. The energy functional for this reads

$$F = \int a + w + f dV \quad (1)$$

$$a = - \sum_{\alpha > \beta} A_{\alpha\beta} \nabla \phi_\alpha \nabla \phi_\beta \quad (2)$$

$$w = \begin{cases} \sum_{\alpha > \beta} B_{\alpha\beta} \phi_\alpha \phi_\beta & \phi \in \Delta^N \\ \infty & \text{else} \end{cases} \quad (3)$$

$$f = \sum h_\alpha(\phi) g_\alpha(c_\alpha) \quad (4)$$

with the phase-field ϕ , its individual components ϕ_α , model parameters A, B which will be shortly related to physical ones, a weighting function $h_\alpha = \phi_\alpha$ and the Gibbs free energy density of each phase g_α in terms of the phase concentration c_α . The potential energy w assigns infinite energy to points outside of the standard n -simplex

$$\Delta^N = \{(\phi_0, \dots, \phi_{N-1}) : \sum \phi_\alpha = 1 \wedge \phi_\alpha \geq 0, \forall \alpha \in \{0, \dots, N-1\}\} \quad (5)$$

in order to obtain a finite interface width.

The time evolution of ϕ is assumed to follow a variational derivative subject to the constraint $\sum \phi_\alpha = 1$. This constraint is built into the time evolution following [12] by a pairwise construction

$$\frac{\partial \phi_\alpha}{\partial t} = \frac{1}{N_z} \sum_\beta L_{\alpha\beta} \left(\frac{\delta F}{\delta \phi_\alpha} - \frac{\delta F}{\delta \phi_\beta} \right) \quad (6)$$

with the pairwise mobility $L_{\alpha\beta}$ and the number of phases N_z which have nonzero gradients at a point. Reducing the above equation for two phases while accounting for the constraint and demanding equilibrium, one obtains an analytically solvable ODE with a solution of the form

$$\phi(x) = \begin{cases} 0 & x \leq -\frac{\pi W}{2} \\ 1 & x \geq +\frac{\pi W}{2} \\ \frac{1}{2}(1 + \sin(\frac{x}{W})) & \text{else} \end{cases} \quad (7)$$

with the interface parameter W , which relates to the interface width $L_\phi = \pi W$. The solution together with demanding that eq. (1) is equal to the interface energy γ when integrated over an equilibrium profile gives $A_{\alpha\beta} = \frac{4W\gamma_{\alpha\beta}}{\pi}$ and

$B_{\alpha\beta} = \frac{4\gamma_{\alpha\beta}}{\pi W}$ assuming a constant W . The phase-field mobility L can be related to the physical mobility by considering a pure system $f = 0$ with an interface whose radius of curvature satisfies $\frac{1}{\kappa} \gg W$. This eventually yields $L_{\alpha\beta} = \frac{\pi M_{\alpha\beta}}{4W}$ after comparing to the sharp interface solution for motion by mean curvature flow with $M_{\alpha\beta}$ being the mobility of the relevant interface. Note that if there are driving forces besides curvature, the law of motion would change, which the formula for the phase-field mobility would need to account for in order to recover the proper kinetics. This is generally done with an asymptotic analysis.

In order to allow for an arbitrary number N of phase-fields to be simulated efficiently, at each point in the domain only a fixed number of phase-fields N_p is stored, in the spirit of [13]. This is allowable due to the finite extent of the phase-field, which takes on trivial values on a large part of the domain. Thus each phase-field cell has N_p phase-fields and integers indicating the phase these belong to, as well as an integer $N_z \leq N_p$ counting phase-fields with non-zero gradients. The number N_p is adjusted to the problem at hand, with the benchmarks comparing to analytical solutions also being cheaply computable without this scheme since there $N \leq 3$. For these cases this storage scheme is unnecessary, but was still used for consistency with the final benchmark of section 4.5 where $N_p = 12$ is employed. The resulting runtimes for benchmarks will thus be larger than if a simple direct $N \in \{2, 3\}$ scheme were to be used; the number of right-hand side evaluations however is unaffected by this. Note that even though N_p phases are formally saved, only the local phases N_z are loaded and used for computation. This is in contrast to remapping schemes such as [14] which need to load and calculate the entire chosen length, even if their update is trivially zero or vanishingly small.

Due to infinite energy outside of the simplex in the energy eq. (3) any ϕ that is calculated has to be within the simplex. This is accomplished by the following trivial projection: For any $\phi_\alpha < 0$, set its value to zero; if any $\phi_\alpha \geq 1$, set it to one and set all other ϕ_β to zero. After this part the $\sum \phi_\alpha = 1$ constraint may no longer be fulfilled, which is accounted for by dividing the ϕ vector by its sum. For the final geometry described in section 4.5 we employ a mobility-based simplex as proposed in [3]. A more detailed investigation of the influence of the chosen simplex together with mobility contrasts is left to future work.

The concentration evolution follows a conservative Cahn-Hilliard ansatz

$$\frac{\partial c}{\partial t} = -\nabla \cdot (-M_c \frac{\delta F}{\delta c}) \quad (8)$$

$$= \nabla \cdot M_c \nabla \sum_\alpha h(\phi_\alpha, \phi) \frac{\partial g_\alpha}{\partial c} \quad (9)$$

with some mobility M_c . As c is the independent variable whereas the Gibbs energies are formulated in their phase concentrations, some additional relation is required. For this the concentration is additionally represented as

$$c = \sum h_\alpha c_\alpha \quad (10)$$

$$\mu_\alpha = \mu_\beta = \dots = \mu \quad (11)$$

$$\mu_\alpha = \frac{\partial g_\alpha}{\partial c_\alpha} \quad (12)$$

i.e. c is a weighted sum of the phase concentrations and local equilibrium is assumed. We may thus simplify

$$\sum_{\alpha} h(\phi_{\alpha}, \phi) \frac{\partial g_{\alpha}}{\partial c} = \mu \quad (13)$$

by using the chain rule and the c derivative of the weighted sum representation. Inserting back into the evolution equation yields

$$\frac{\partial c}{\partial t} = \nabla \cdot M_c \nabla \mu \quad (14)$$

$$= \nabla \cdot \sum_{\alpha} (D_{\alpha} h_{\alpha} (\frac{\partial^2 g_{\alpha}}{\partial c_{\alpha}^2})^{-1} \nabla \mu) \quad (15)$$

$$= \nabla \cdot \sum_{\alpha} (D_{\alpha} h_{\alpha} \nabla c_{\alpha}) \quad (16)$$

in which the form for $M_c = \sum_{\alpha} D_{\alpha} h_{\alpha} (\frac{\partial^2 g_{\alpha}}{\partial c_{\alpha}^2})^{-1}$ is chosen such that it cancels the relevant part from $\nabla \mu = \frac{\partial^2 g_{\alpha}}{\partial c_{\alpha}^2} \nabla c_{\alpha}$. The last line writes out the sum and then replaces $\nabla \mu$ with its equivalent in terms of ∇c_{α} before moving back into sum form. One can thus interpret the concentration evolution as a weighted average of phase-diffusion problems. The phase-wise concentrations c_{α} may be obtained from solving the system described by eqs. (10) and (11).

We employ parabolic Gibbs free energies of the form

$$g_{\alpha} = \frac{k_{\alpha}}{2} (c_{\alpha} - c_{0,\alpha})^2 \quad (17)$$

and distinguish up to two phases α, β with β assumed to be a solid which can take on many orientations while employing the same chemical energy. The associated grand potential is

$$\psi_{\alpha} = g_{\alpha} - \mu c_{\alpha} = -\frac{\mu^2}{2k_{\alpha}} - \mu c_{0,\alpha}. \quad (18)$$

3. Methods

In this section the time integrators used to solve eqs. (6) and (16) are introduced together with some additional implementation details. The numerical framework used for the investigation supports execution on both the CPU and GPU, with parallelization achieved using the Message Passing Interface (MPI). It will be detailed in another publication. Spatial discretization is generally carried out with second order finite differences, with divergences being resolved as a sum of flux differences between faces. Point values are laid out on a cell-centered regular Cartesian grid with spacing Δx , with each unknown in a cell representing a degree of freedom (DoF).

3.1. Temporal discretization

A variety of explicit temporal integrators is evaluated in the present paper, with a short overview given in the present section. Among them is the “standard” forward Euler integrator as used by many explicit phase-field codes as a

reference to how much faster other integrators may be; integrators suited for integration together with advective terms as their stability region includes a part of the imaginary axis (SSP schemes); and finally unconditionally stable explicit integrators built for parabolic problems (STS schemes). STS schemes are chosen as they allow for more efficient time integration for semi-stiff problems and SSP schemes for potential inclusion of advective terms, which will be the focus of a later work. SSP schemes may also be seen representative of “normal” Runge-Kutta methods which improve temporal accuracy but do not gain computational efficiency (no. RHS evaluations vs. stability limit) over the forward Euler integrator.

For this section we consider PDEs of the form

$$\frac{\partial u}{\partial t} = f(u, \nabla u, \nabla^2 u, \dots) \quad (19)$$

$$\frac{\partial u}{\partial t} \approx \text{rhs}(u(t)) \quad (20)$$

with a finite difference semi-discretization being carried out in transforming the continuous right-hand side f into its semi-discrete part rhs .

The simplest integrator considered is the forward Euler (FE, FEuler) integrator given by

$$u^{n+1} = u^n + \Delta t \text{rhs}(u^n) + \frac{1}{2} \Delta t^2 \frac{\partial^2 u}{\partial t^2} + O(\Delta t^3) \approx u^n + \Delta t \text{rhs}(u^n) \quad (21)$$

with a local error of $O(\Delta t^2)$ and so global error order 1. Its stability limit can be determined from the Dahlquist test equation and its corresponding discretization

$$\begin{aligned} \frac{\partial u}{\partial t} &= \lambda u \\ u^{n+1} &\approx (1 + \Delta t \lambda) u^n = R(\Delta t \lambda) u^n \end{aligned} \quad (22)$$

in which the stability polynomial $R(\Delta t \lambda)$ is introduced. Explicit Runge-Kutta (RK) methods may always be written in the form eq. (22), with the only difference being the expression for R . In order for a method to be absolutely stable, i.e. errors introduced earlier do not grow exponentially, the bound[15]

$$|R| < 1 \quad (23)$$

has to be satisfied, which for the above test equation (assuming $\lambda < 0$ for notational simplicity) is the case for

$$\Delta t_e < \frac{2}{|\lambda|}. \quad (24)$$

We also consider two strong positivity preserving (SSP) schemes, namely SSP(n)2 and SSP(10)4, which are respectively an n -stage scheme of order 2 and a 10-stage scheme of order 4. These schemes are efficient and accurate integrators for advective terms. The implementation is similar to the one given in [16] except that an explicit additional vector is used since fulfilling the storage assumption is quite difficult on GPUs. Following the cited work, we have the

stability limits

$$\Delta t_{SSP(n)2} < \frac{n-1}{n} \Delta t_e \quad (25)$$

$$\Delta t_{SSP(10)4} < 6\Delta t_e \quad (26)$$

with Δt_e being the stable FE step as derived previously.

Finally, super timestepping (STS) schemes of order 1 and 2 are also considered within the work. Either scheme with s stages may be written in the general form

$$u^{n,0} = u^n \quad (27)$$

$$u^{n,1} = u^{n,0} + \tilde{\mu}_1 \Delta t \text{rhs}(u^{n,0}) \quad (28)$$

$$\begin{aligned} u^{n,j} = & (1 - \mu_j - \nu_j)u^{n,0} + \mu_j u^{n,j-1} + \nu_j u^{n,j-2} \\ & + \Delta t(\tilde{\mu}_j \text{rhs}(u^{n,j-1}) + \tilde{\gamma}_j \text{rhs}(u^{n,0})) \end{aligned} \quad (29)$$

$$u^{n+1} = u^{n,s} \quad (30)$$

with schemes of order 1 having $\nu_j = 0, \tilde{\gamma}_j = 0$. The coefficients $\mu_j, \nu_j, \tilde{\mu}_j, \tilde{\gamma}_j$ depend on the chosen stability polynomial basis and the order of the scheme. A common feature however is that the stable time step scales as

$$\Delta t = k \Delta t_e s^2 \quad (31)$$

i.e. quadratically in the number of stages s relative to the stable FE step (largest eigenvalue). Thus these schemes can be said to be unconditionally stable, as one might simply choose a large number of stages to achieve the desired stability limit. Choosing a larger step also makes the scheme more efficient relative to the FE scheme as increasingly fewer RHS evaluations will be required; this is in contrast to the SSP(n)2 scheme, whose stability domain only grows linearly. Within this work we only consider the Lagrange basis introduced by [17, 18] for simplicity; the general trends should follow for other bases, with a possible exception of a Chebyshev basis when using spatially variable coefficients, as these may introduce step artifacts in the solution[18]. In order to estimate the stable Euler time step Δt_e necessary to compute the stable number of stages via eq. (31), we employ Gershgorin's circle theorem on eqs. (6) and (16) separately for a two-phase system. This results in estimates λ_ϕ, λ_c which are detailed in the supplementary material. The larger of the two resulting eigenvalues is then used to estimate a stable Euler step $t_e = \frac{2}{\lambda}$, which is multiplied by a safety factor of 0.9 before being used to estimate the stage number, which is rounded to the next largest odd number as even stage numbers fail at damping short wavelengths[17]. If a problem only involves the phase-field, as in section 4.3, only the phase-field eigenvalue estimate is employed without terms relating to the chemical driving force. For simplicity no nonlinear power method was used for estimating the eigenvalues; for more complicated couplings in which Gershgorin's circle theorem yields very crude bounds or involves substantial linearization it may also speed up the computation by allowing larger steps.

The simplex constraint of the phase-field suggests one deviation from the STS2 scheme: If in the first stage the new phase-field values exceed the simplex constraint, adding the same RHS again later will most likely continue to trigger

the simplex, introducing additional error. Thus, if this case is detected, then $\text{rhs}(u^{n,0})$ is re-computed as

$$\text{rhs}(u^{n,0}) = \frac{S(u^{n,1}) - u^{n,0}}{\tilde{\mu}_1 \Delta t} \quad (32)$$

with S being the simplex projection operator. The effective initial RHS is one s.t. the simplex constraint is not violated. In computational experiments this significantly improved the error behaviour.

3.2. Temporal adaptivity

For conditionally stable schemes, often a time step close to the stability limit is chosen for reasons of computational efficiency, with the hope being that the temporal error introduced thus is much smaller than the spatial error. However, for unconditionally stable schemes some kind of adaptivity is necessary as to decide what step size to take. For this an estimate of the local error introduced by the time stepping process is useful. The SSP methods are extended with the embedded solution coefficients of [19] and thus they can estimate the error at little extra computational cost but with one extra vector being stored. For the STS methods, the error may be estimated following [20] requiring an extra RHS evaluation before a time step is accepted¹ but without extra storage requirements. The error formula is then

$$e_u^n = \frac{1}{15} (12(u_i^{n+1} - u_i^n) + 6\Delta t(\text{rhs}(u_i^n) + \text{rhs}(u_i^{n+1}))) \quad (33)$$

which effectively calculates a scaled solution estimate for step $n + 1$, which for the phase-field needs to be subject to simplex constraints. In order to account for this, the phase-field error components are locally filtered: Any component of a trial solution $\tilde{u}(t + \Delta t) = u^n + \frac{\Delta t}{2}[\text{rhs}(u^n) + \text{rhs}(u^{n+1})]$ which lies outside of $[0, 1]$ is assumed to have zero error. Once a phase-field value leaves this interval, it is reasonable to assume that it will not immediately enter it again, as the phase-field describes the advance of a free boundary.

In either case, once a local error estimate e_i^n is available, the error of this step is calculated as

$$e^n = \left[\frac{1}{N} \sum_i \left| \frac{e_i^n}{r \max(u_i^n, u_i^{n+1}) + a} \right|^2 \right]^{\frac{1}{2}} \quad (34)$$

by computing a weighted l^2 norm of the error over all DoFs i . The weight is calculated with a relative tolerance r and an absolute tolerance a to define the level of acceptable error. These tolerances are defined per independent field, i.e. r_ϕ, a_ϕ for the phase-field and r_c, a_c for the concentration. However, since the components of the phase-field are tightly coupled via the simplex and sum constraints, with values to 1 and 0 occurring at the same location, the absolute phase-field tolerance a_ϕ will be varied within the work and its influence mentioned where appropriate..

¹This evaluation might be re-used for the first stage of the next step if it's accepted; for simplicity this wasn't implemented and the additional RHS evaluations were counted.

If $e^n < 1$, the step is accepted, otherwise rejected. In either case, a new time step is calculated following the PID-controller of [21] together with a bias $b \in [0.1, 0.98]$ and the local order P of the method

$$E_n = e^n / b \quad (35)$$

$$F = (E_n^{-k_1} E_{n-1}^{-k_2} E_{n-2}^{-k_3})^{1/(P+1)} \left(\frac{\Delta t_n}{\Delta t_{n-1}} \right)^{k_4} \left(\frac{\Delta t_{n-1}}{\Delta t_{n-2}} \right)^{k_5} \quad (36)$$

$$\Delta t_{n+1} = \Delta t_n \left(1 + 5 \arctan \left(\frac{F-1}{5} \right) \right) \quad (37)$$

with $k_1 = 1.25, k_2 = 0.5, k_3 = -0.6, k_4 = 0.25, k_5 = 0$; note that the step index is now a subscript as not to be confused with the exponentiation. The bias b starts at 0.9 and makes the step estimate slightly more conservative; it is multiplied by itself on step rejection to make successive step rejections more unlikely, up to a value of 0.1. On step acceptance, it is divided by \sqrt{b} but limited to 0.98. The time step factor F is then smoothed to limit the overall step size changes. Terms for which there is no data yet are dropped from the above expression. We observed that the full controller may suggest increasing the time step upon rejection; in this case only $e_n^{-k_1/(P+1)}$ is used for estimating the new timestep, which is certain to decrease the time step.

The compact support of the phase-field and its storage scheme impacts the definition of N within eq. (34). For a vectorial unknown X with k components, $N = V k$ trivially with V being the number of points in the domain. Using this definition would massively underestimate the error, as most entries of the phase-field will attain trivial values and hence have zero error. Hence we only count nontrivial entries, which are defined as having nonzero e_i^n . Furthermore, due to the compact support there may be entire regions for which there are zero nontrivial DoFs. In order to stay somewhat comparable to well-types of potentials, a zero nontrivial phase-field cell is treated as 2 DoF, since a direct two-phase implementation would simply have two DoFs per cell. In these cases one would have a nonzero but vanishingly small error in these regions, which should be somewhat comparable to the present approach. A more detailed investigation, e.g. only accounting for errors for the phase-field in the interface, is left to future work.

We note that reductions, such as required by the error estimator, are non-deterministic on GPUs[22] and so the runtimes and RHS counts can slightly fluctuate when using an adaptive time step on GPUs. While this also applies to MPI parallel reductions, the number of non-associative operations is often far smaller and so can usually be ignored.

3.3. Error sources

There are many kinds of errors when integrating a PDE numerically; this section shall serve as a small overview of the errors considered within the work. First there are discretization errors, in both the space and time dimension, induced by the discretization schemes. Their order can generally be determined analytically, with a concrete value requiring knowledge of the solution or computational experiments as they relate to the derivatives of the solution. We will generally consider both. Note that spatial and temporal error can compensate each other and thus conditions which should have larger temporal error can in fact end up with smaller total error. Next, when working with floating point

arithmetic there is necessarily some amount of error involved in mapping the infinite real numbers into a finite set. We generally do not consider these to be significant, as the quantities we compute are scaled to be $O(1)$ such that the floating point error should be far below the discretization error. Finally, an error specific to phase-field methods is that originating from the finite interface width, which manifests in a deviation from the target free-boundary problem. When only comparing to reference solutions at refined space/time grids, this error does not play a role, but is critical for matching the physics of a problem. Generally, lower interface widths produce less error, but the spatial discretization interacts with the interface width and hence some care is required when performing grid convergence studies and comparing against free-boundary problems.

The spatial discretization error for the Laplacian of the equilibrium phase-field profile eq. (7), away from the bulk, scales as

$$e_{\Delta x} \propto \sum_{n=1} q_n \frac{\Delta x^{2n}}{W^{2+2n}} \quad (38)$$

and thus, in order for the error to vanish as $\Delta x, W \rightarrow 0$, the terms $\frac{\Delta x^{2n}}{W^{2+2n}}$ need to go to zero. For constant W , one obtains the usual error order if a reference solution using a sufficiently small Δx is employed. However, this does not necessarily recover the sharp interface limit $W \rightarrow 0$ of the free-boundary problem. Thus, when doing grid convergence studies, W is chosen as $W = 3\Delta x^m$ with $m = 0.4 < \frac{1}{2}$ for which the above error goes to zero for any n . The prefactor is chosen such that at the coarsest resolution employed we have about 9 cells in the interface. The error w.r.t. the sharp interface solution does not necessarily follow a simple power law, since it is the combined error of discretization and from the diffuse interface.

4. Benchmark geometries and parametrization

In this section the benchmark geometries will be introduced, along with how the error for each one will be estimated. The benchmarks are generally chosen such that an analytical solution for the equivalent free-boundary problem exists. This allows us to determine when spatial or temporal error dominate as well as what kind of tolerances can be appropriate. Furthermore, the parameters employed for the simulation will be detailed.

In most cases, the initial conditions of the phase-field are based on calculating the profile function eq. (7) with a suitably defined distance field d as its argument. Thus only the distance field d will be given for these cases. If a simulation includes eq. (16), then the initial concentration field is given by the local equilibrium eq. (10) unless mentioned otherwise. If not mentioned otherwise, all boundary conditions are periodic.

An important part of the phase-field theory is that the derived PDEs represent gradient flows of an energy functional. This ensures that the evolution minimizes that functional. Schemes ensuring this are generally referred to as energy stable[23], with many classical schemes not being unconditionally so. In lieu of proving (conditional) energy stability for schemes employed herein, two cases with analytical equilibrium state are considered. Even if the schemes should temporarily have increasing energy (as shown), it is deemed acceptable

if the analytical equilibrium state is the convergence point of a grid refinement study and that at a practical resolution, the scheme approximates the equilibrium state closely as well. Note that all schemes employed here contain at least one (scaled) forward Euler step and hence would at best be conditionally energy stable. We further note that even energy stable schemes might not lead to the correct kinetics[7], so they should also be benchmarked before use.

As equilibrium states should be independent of the choice of kinetic parameters, ignoring discretization error, unconditionally stable schemes can speed up convergence somewhat: To a first approximation, the time to equilibrium depends on how fast a homogeneous chemical potential is reached, which scales with the driving forces and diffusivity. The phase-field mobility only enters the problem insofar as moving the interface, following the diffusion field. Thus increasing the diffusivity can reduce the time required to reach equilibrium. Note that if all kinetic parameters are increased by the same factor, nothing is gained as this simply rescales the time for the system.

The standard set of parameters employed is shown in Table 3, which will be used unless mentioned otherwise; these do not represent any specific material. For equilibrium simulations, $D = 100$ is used to speed up convergence.

Table 1: employed parameters

parameter	value
M	1
γ	1
W	2.5
Δx	1
D	1
$k_\alpha = k_\beta$	500
$c_{0,\alpha}$	0.02
$c_{0,\beta}$	0.98

Finally, the values used for equilibrium determination in the benchmarks sections 4.1 and 4.2 may oscillate around a steady-state value. In order to account for this, an oscillation resistant-algorithm detailed in the supplementary material is employed.

4.1. Phase embedding

The first case is that of one phase being embedded in another, with curvature providing a driving force for shrinkage which is counteracted by chemical driving forces. Both phases are initialized with their flat equilibrium concentration values and thus there is a small driving force for diffusion in order to reach equilibrium in which there is a pressure difference, the Laplace pressure,

$$\Delta P = \gamma \kappa \quad (39)$$

between both phases, with the curvature κ . This pressure difference is achieved by a shift in chemical potential via mass transfer. In order to accommodate this mass transfer, the volume of the individual phases changes slightly. The curvature is determined from a shape assumption, e.g. for a circular embedding

we have $\kappa = \frac{1}{r}$ with r being the radius of the embedded phase. The pressure difference is equivalent to the difference in grand potentials $\Delta\psi$ of the bulk phases in equilibrium, as this is the driving force resisting capillary pressure. The bulk grand potentials are defined as the values the respective grand potentials take on at the average chemical potential of the domain. Hence the error is defined as

$$e = |\gamma\kappa - \Delta\psi|. \quad (40)$$

The distance field for the inner phase is

$$d = r - \|X - C\|_2 \quad (41)$$

with the position vector X , the center of the system $C = (\frac{L_1}{2}, \dots)$ and the initial radius of the phase r . The outer phase follows as the complement.

We note that resolving a discretized profile with different interface widths tends to produce slightly different areas after integration, as there is some error associated with the interface width (see the supplementary material for details). This also affects the concentration in the domain, which in turn affects the equilibrium. In order to counteract this, the difference of the sharp-interface concentration $C = V_e c_e + V_E c_E$ (with the sharp interface volumes V_e and V_E of the embedding/embedded phases) to the concentration in the domain $\int_V c dV$ is used to shift all concentration values in the domain by their difference divided by the volume of the domain. This is also done for the next benchmark.

4.2. Double triple junction

The second case is a triple junction geometry, now also probing variable parameters and multiple phases interacting. One phase α is placed on the grain boundary between two grains of the phase β , as sketched in fig. 1 together with the employed boundary conditions and geometric quantities, forming two triple junctions. In contrast to [3], we want to test the equilibrium together with a chemical driving force, and so do not require Dirichlet boundary conditions to prevent curvature minimization from eliminating all interfaces. We note that this choice generally leads to much longer simulation times, as the equilibrium is now linked to the long-range diffusion field. The evolution should be such that the phase α obtains an equilibrium shape defined by the dihedral angle

$$\theta_{eq} = 2 \arccos\left(\frac{\gamma_{\beta\beta}}{2\gamma_{\alpha\beta}}\right) \quad (42)$$

with its momentary form being calculable with the geometric parameters L , S following [24] by assuming the shape is a vesica piscis:

$$\theta = 4 \arctan\left(\frac{S}{L}\right). \quad (43)$$

These parameters are estimated based on the extremal extents of the 0.5 level set of phase α . The error is then simply defined as

$$e = |\theta_{eq} - \theta|. \quad (44)$$

The geometric description based solely on distance fields somewhat breaks

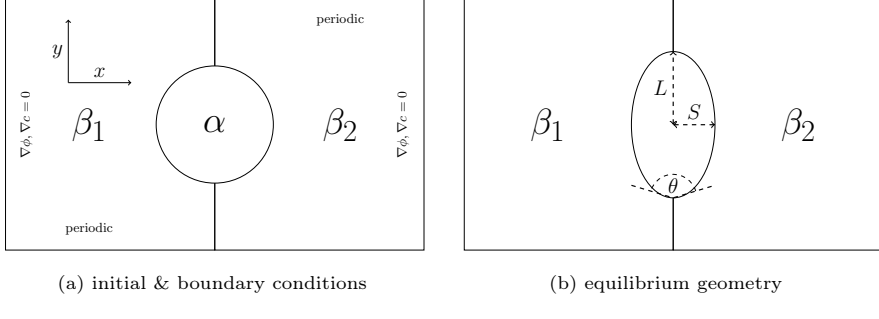


Figure 1: Geometry for the double triple junction.

down here as there are multiple overlapping ones which do not sum to 1. We consistently proceed as follows: We want the phase α to exactly follow the distance field $d_\alpha = r - \|X - C\|_2$ and thus we can fix its value $\phi_\alpha = \phi(d_\alpha)$. The distance field of the left grain is given by $d_1 = C_x - x$; this is used to calculate $\phi_1 = \phi(d_1)$ and $\phi_2 = 1 - \phi(d_1)$. In order to account for equivalence of the geometry without the α phase, the ratio $q_{12} = \frac{\phi_1}{\phi_2}$ should be preserved and the sum constraint $\phi_2 + \phi_1 = 1 - \phi_\alpha$ should be fulfilled to keep ϕ_α constant. This results in a system of equations which can be solved for new values of ϕ'_2, ϕ'_1 satisfying these restrictions. Note that while it appears nonlinear, row-wise multiplication by the divisor allows for transformation to the equivalent linear system for any N :

$$\begin{bmatrix} 1 & -q_{12} & 0 & \cdots & 0 \\ 0 & 1 & -q_{23} & \cdots & 0 \\ \vdots & \vdots & \vdots & \vdots & \vdots \\ 1 & 1 & 1 & \cdots & 1 \end{bmatrix} \begin{bmatrix} \phi'_1 \\ \phi'_2 \\ \vdots \\ \phi'_N \end{bmatrix} = \begin{bmatrix} 0 \\ 0 \\ \vdots \\ 1 - \phi_\alpha \end{bmatrix}.$$

4.3. Single grain growth

A single grain embedded within another grain will shrink due to excess energy contained in the interface, given that there are no other driving forces preventing this. Assuming that curvature flow is the only active mechanism, one may write for the volume of the embedded grain

$$\frac{\partial V}{\partial t} = - \int_{\partial V} v dA \quad (45)$$

$$= - \int_{\partial V} M \gamma \kappa dA \quad (46)$$

with the grain mobility M , the interface energy γ and the curvature κ . For a particular dimension and object shape the ODE can be solved analytically, say in two dimensions for a circle, resulting in:

$$r(t)^2 - r(0)^2 = -2M\gamma t \quad (47)$$

$$A(t) - A(0) = -2M\pi\gamma t \quad (48)$$

which gives us an exact solution to compare to, with the last line not even requiring any shape assumption anymore. As the time derivative of the area

should be constant, the error may naturally be defined as

$$e = \left| \frac{\partial A_{num}}{\partial t} - (-2M\gamma\pi) \right| \quad (49)$$

with the numerical derivative being the average for $t > 0$ of a 2nd order finite difference derivative of the respective data. This time filter is applied to exclude the early adjustment from the ideal to a numerical profile.

In this case only the phase-field equation eq. (6) is solved for, as both grains are of the same phase. The inner grain uses the distance field eq. (41), with the outer one being the complement. The area of the grain follows from simple volume integration.

4.4. Solutal Stefan problem

The second kinetic test approximates the classical Stefan problem in a solutal setting. Two semi-infinite phases α and β are brought into contact with respective initial compositions c_α , c_β . If these differ from their equilibrium composition, then the interface between them will move. Following [25], employing a similarity solution for the diffusion fields and incorporating the flux balance at the interface as well as assuming equal atomic volumes and diffusivities D , yields

$$X(t) = A\sqrt{t} \quad (50)$$

$$A = \sqrt{\frac{4D}{\pi}} \left[\frac{c_\alpha - c_{\alpha\beta}}{c_{\beta\alpha} - c_{\alpha\beta}} \frac{\exp(-A^2/(4D))}{1 - \operatorname{erf}(A/\sqrt{4D})} \right. \\ \left. + \frac{c_\beta - c_{\beta\alpha}}{c_{\beta\alpha} - c_{\alpha\beta}} \frac{\exp(-A^2/(4D))}{1 + \operatorname{erf}(A/\sqrt{4D})} \right] \quad (51)$$

for the interface position X and the growth parameter A , with the concentrations on the α and β side of the interface $c_{\alpha\beta}$ and $c_{\beta\alpha}$. Assuming that these interface concentrations match the equilibrium concentrations is equivalent to saying that the generalized Gibbs-Thomson effect vanishes, i.e.

$$\Delta\mu = \Gamma\kappa + Kv = 0 \quad (52)$$

with suitably defined Gibbs-Thomson coefficient Γ and kinetic coefficient K . Employing a one-dimensional geometry ensures κ vanishes. Since $v > 0$ is required for kinetics, we are left with making K vanish by determining its relation to the phase-field parameters. The latter is usually done with a thin-interface analysis; for details, refer to e.g. [26]. A relationship for the phase-field mobility L

$$L = \frac{\pi^2}{16W^2} \frac{D \frac{\partial c}{\partial \mu}}{(c_\beta^{eq} - c_\alpha^{eq})^2 (M + F)} \quad (53)$$

is eventually obtained for $K = 0$, with the terms $M + F \approx 0.3084251$ being integrals involving the weighting function h as well as the phase-field profile. Note that with the assumption of equal diffusivities there is no need to include an anti-trapping current. Furthermore, the prefactors k in the Gibbs energies

in eq. (17) are reduced to 1 as to allow sufficient solubility in the phases, which is required by the long-ranged smooth concentration fields.

The error is defined with the help of A^* , obtained from fitting the simulated interface position-time data to eq. (50), as

$$e = |A - A^*|. \quad (54)$$

The distance field for phase β is given by $d = h - x$ for an initial height h from the left boundary, with that of α being the complement. The initial concentration is interpolated as $c(t=0) = \phi_\alpha c_\alpha + \phi_\beta c_\beta$, i.e. the far-field phase concentration values are employed. For the phase-field, gradient zero boundary conditions are employed, whereas the boundary concentrations are held at the respective initial concentrations with Dirichlet conditions.

We note that there is an additional error source here compared to the other benchmark geometries, namely the far-field concentration. For the analytical solution an infinite domain is assumed, which obviously cannot be simulated. Hence one must ensure that the gradients in the far field are negligible. We chose a time giving a certain displacement $X(t) = 50 \rightarrow t \approx 43 \times 10^3$ via eq. (50) and then varied the physical domain size in an informal study to fix it for the reported simulations. Finally, the momentary position $h + X(T)$ is determined based on the position of the $\phi_\alpha = 0.5$ point determined via solving a cubic interpolant.

4.5. Grain growth with particles

As an application example we will also treat a system which doesn't have an analytical solution, but which is representative of more typical ratios of kinetic parameters as well as more complicated geometries. For this a system of many grains β of different orientation is employed, together with spheres of a second phase α randomly placed in this structure. When these second phases are in contact with a grain boundary, they exert a drag force on the boundary. Depending on the effective mobility of the second phase, these may be taken to be immobile particles which act as pinning centers, allowing for investigations relating to Zener pinning and limiting grain sizes. For more mobile phases, this represents the final stage of sintering with only closed porosity remaining, which reduces grain growth but does not necessarily lead to a limiting grain size, as pores may move and end up merging. The effective particle mobility can be controlled via the size of the second phase and the diffusivity controlling the mass transport[27], which for simplicity here was taken to be diffusion within the second phase, i.e. vapour diffusion if we interpret it as a pore. We note that Zener pinning can in general be more easily simulated without recourse to using a concentration field, see e.g. [28]. The final sintering stage can also be approximated without diffusion fields, see e.g. [29], but this assumes known dominant diffusion mechanisms, more materials parameters and a tracking algorithm to account for pore pressure and pore-pore interactions. Furthermore, pores in the final sintering stage can also be elongated, in which case diffusional instabilities such as the Plateau-Rayleigh instability become relevant. These are more easily described by employing concentration fields. We note that the eventually chosen parametrization for this case may be calculated more efficiently by integrating the phase-field and concentration fields separately, as their respective

timescales differ by several orders of magnitude; but for ease of presentation and comparability both fields were integrated together.

We seek to reproduce the following qualitative behaviours with three simulations: If grain growth without particles happens, mean-field theory based on curvature as the sole driving force predicts parabolic growth of the mean grain size, i.e. $G(t)^n - G(0)^n = kt, n = 2$ [1]. As alluded to in the previous paragraph, immobile particles can lead to a limiting grain size, which in experiments may also be identified as large exponents n since the curve will tend to flatten out increasingly. In contrast to this, while mobile particles (pores) also exert a drag force on the grain boundary, they co-move with the grain boundary and may merge with others, reducing their effectiveness as pinning centers. Hence in this case the exponent generally increases, see e.g. [30, 31], while not necessarily reaching a limiting grain size. Based on the different parameters here we will be able to observe speedups for realistic parameter combinations.

The initial conditions for pure grain growth are a periodic Voronoi tesselation of 3D space with random points, with a minimal distance of $12\Delta x$ between each point of a $(400\Delta x)^3$ domain. Once this simulation has reached a roughly parabolic regime ($t = 1$ in the computational experiments) simulations with particles are constructed based on this configuration: For immobile particles, spheres are placed randomly in space with a target volume ratio $f_i = 0.15$ and radius $r_i = 6\Delta x$ in order to showcase the limiting grain size, with the distance between spheres being at least $d = 2r$. Due to the finite extent of the phase-field this still means that some overlap exists, which does increase the effective radius but due to the low mobility the particles do not move or change shape over the simulation duration. However, for mobile particles this would lead to quick merging of most particles, giving a completely different geometry than expected. Hence for these a minimal distance of $d = 2(r + e), e = 8\Delta x$ is imposed, which limits the obtainable porosity as a function of this distance and the pore radius. Due to this limit we pick $f_m = 0.05, r_m = 10\Delta x$ which is also more representative of the porosity in final stage sintering. While it is possible to also calculate the immobile particle case with this particle distribution, the simulation domain would need to be enlarged significantly to reach the limiting grain size. For the immobile parameters the classical Zener pinning theory predicts a limiting grain size of $r_{l,i} = \frac{4}{3} \frac{r}{f} \approx 53.3\Delta x$ whereas for the mobile particle distribution it would be $r_{l,m} \approx 266\Delta x$ and hence require a domain in excess of $(800\Delta x)^3$ [32]. While calculating such a domain poses no problems but the waiting time for the employed code, the goal of reproducing qualitative behaviour does not necessarily justify the simulative expense.

We note that the phase-field volume $\int_V \phi(d) dV$ of a two and higher dimensional shape has an $O(W^2)$ error compared to the sharp interface volume the distance field d is supposed to represent. In order to still obtain a porosity close to the target porosity even when the size of the particles is comparable to the interface width, the radius r is transformed to a smaller equivalent radius r_c such that the target volume is obtained with the help of a function function $r_c = f(r, W)$ derived in the supplementary material. With the centers and radius of the particles fixed, the only thing left is to place them in the domain. Since a diffuse initial shape is used, $\phi_\alpha = \phi(r_c - x_{min})$ is imposed for each cell while keeping the ratios of the remaining phase-fields constant as detailed in section 4.2. x_{min} here is the smallest distance of this cell to any of the particle positions. The geometry is hence fully described and what remains is to fix the

parameters representing the different regimes.

For insoluble, mobile particles (pores) we want small particle in some sense with sufficient diffusivity. Since the mobility of these scales as $r^{-n}, n > 2$ [27] with the particle size r , choosing a smaller length scale means we have more mobile particles relative to pure grain growth. At the same time, we would like to use the same length scale for immobile particles, hence after fixing the length scale, diffusion values leading to immobile and mobile particles are determined. Furthermore, in order for the particles to be insoluble even under capillary action the prefactor k in eq. (17) needs to be large relative to capillary forces. We can estimate this effect by considering the expression for the phase concentration in terms of the chemical potential $c_\alpha = c_{0,\alpha} + \frac{\mu}{k}$ and the equilibrium condition $\psi_\alpha - \psi_\beta = \gamma\kappa$, from which we find that the shifted equilibrium bulk concentration is $c_\alpha(\gamma\kappa) = c_{0,\alpha} - \frac{\gamma\kappa}{k(c_{0,\alpha} - c_{0,\beta})}$. We would like for the difference to the bulk concentration to be small relative to the bulk concentration, and hence must know the scale of $O(\kappa) = O(\frac{1}{r})$. By computational experiments we pick a length scale of $\Delta x = 0.005$ at which $D_\alpha = 10$ shows visibly mobile particles and hence $k = 1 \times 10^5$ ensures $\frac{c_\alpha(\gamma\kappa) - c_{0,\alpha}}{c_{0,\alpha}} < 1\%$ for the considered particle sizes.

The grain boundary mobility is set to be $M_{\beta\beta} = 5 \times 10^{-3}$. The diffusivity within grains is taken to be $D_\beta = 5 \times 10^{-8}$ as a small number effectively suppressing Ostwald ripening on the considered time scale. For immobile particles $M_{\alpha\beta} = 5 \times 10^{-8}, D_\alpha = 5 \times 10^{-8}$ are chosen as to make the particles immobile on grain growth time scales. Finally, with $M_{\alpha\beta} = 5 \times 10^{-3}, D_\alpha = 10$ mobile particles are realized.

If the immobile particle parameters are employed directly after setting the particles, stable many phase regions tend to form on the fringes of the particles, even if a simplex accounting for mobility variations is employed as suggested in [3]. We suspect that this is due to chemical driving forces aiming to shrink the particles to achieve their capillary equilibrium, which gives a driving force to any grain phases in the vicinity. This driving force may exceed the potential energy terms of the phase-field and hence stabilize many phase regions which originally exist due to the interface width being comparable to some of the initial grains' equivalent radius. While these would eventually vanish after capillary equilibrium is achieved, the timescale for that is far beyond the timescale of grain growth for this parameter combination. Since these may act as artificial pinning centers, an additional equilibration run is conducted for both particle-laden simulations prior to running with the actual parameters. The run uses $M_{\beta\beta} = 5 \times 10^{-8}, D_\alpha = 5 \times 10^{-3}, M_{\alpha\beta} = 5 \times 10^{-3}$ as to ensure that virtually no grain growth happens while at same time allowing for capillary relaxation, and is continued for a duration of 5 time units. After this equilibration run the time is reset to $t = 1$ and the simulations are run normally; no further formation of stable many phases regions was observed.

5. Results

In this section the results of the simulations studies are presented. We first ascertain whether the STS time integrator approximates the sharp interface limit for equilibrium configurations. This is followed by determining whether the kinetics are matched as well, together with a performance comparison between probed integrators. Performance is reported here in terms of RHS evaluations,

as this measure is independent of the machine employed and hence eases future comparison with other time integrators. Qualitative comparison to implicit integrators can also be done with this as long as the resulting systems are solved with iterative methods as each iteration requires RHS evaluations; a more quantitative comparison needs to account for e.g. additional matrix-vector operations required by the solution algorithm as well as potential mass matrix inversions. The supplementary material includes data on the runtimes as well for the interested reader, though the conclusions do not change if performance is measured in runtime instead of RHS evaluations.

The main set of integrators with their configurations is described in Table 2. If not mentioned otherwise, adaptive integrators use tolerances of $a = 1 \times 10^{-4}$, $r = 1 \times 10^{-4}$ for all fields. For grid convergence studies, only the STS2 integrator with $a_\phi \in \{1 \times 10^{-2}, 1 \times 10^{-4}\}$ is employed to reduce computational expense. The SSP(10)4 integrator at tolerances of 1×10^{-14} is generally used as a reference solution generator for testing convergence order.

Table 2: Employed integrator configurations

integrator	configurations
FEuler	$\Delta t \in \{0.5, 1\} \cdot \Delta t_e$
SSP(5)2	$\Delta t \in \{0.5, 1, 2, 4\} \cdot \Delta t_e$
SSP(10)4	$a_{\phi,c} = 1 \times 10^{-14}$, $r_{\phi,c} = 1 \times 10^{-14}$
STS[12]	$\Delta t \in \{1, 10, 100, 200\} \cdot \Delta t_e$ $a_\phi \in \{1 \times 10^{-2}, 1 \times 10^{-3}, 1 \times 10^{-4}\}$

Finally, we generally output at defined target times exactly. For fixed-step integrators this only manifests in an extra RHS evaluation for each output time not being an integer multiple of the time step width. For adaptive integrators, this generally reduces the step taken prior to reaching the output significantly and hence becomes less efficient than if a simple time crossing output strategy were adopted. Hence the performance results are slightly biased against adaptive integrators.

5.1. Equilibrium verification

First, we perform a mesh convergence study with the geometry of section 4.1, resolving a domain of 128^2 with an initial seed of size $r = 32$. Equilibrium for this case is defined as a rate of change for the Laplace pressure $|\frac{(\Delta p(t) - \Delta p(t_b))}{t - t_b}|$ being smaller than 1×10^{-14} for two times $t > t_b$ at least two diffusion times $128^2/D$ apart.

The results of this study in terms of the error and energy evolution are shown in fig. 2. The inset shows the spatial distribution of the grand potential ψ in equilibrium, showing a clear delineation between the two phases. We observe convergence, though not at a uniform rate. At the coarsest resolution, a relative error of about 1% ($\Delta p_{eq} \approx 0.031$) is obtained, suggesting the equilibrium can also be well-approximated with coarse resolutions as often employed in phase-field studies. Note that the results for the two different absolute tolerances a_ϕ effectively overlap, suggesting the time integration error is negligible. For this case a monotonic decrease in energy is observed, with the energy change after the first output frame being very small; hence in fig. 2(b) only the change in energy

relative to this frame is shown. 0 to 2% of steps were rejected, though given that about 50 steps were calculated, this is likely just the initial adjustment.

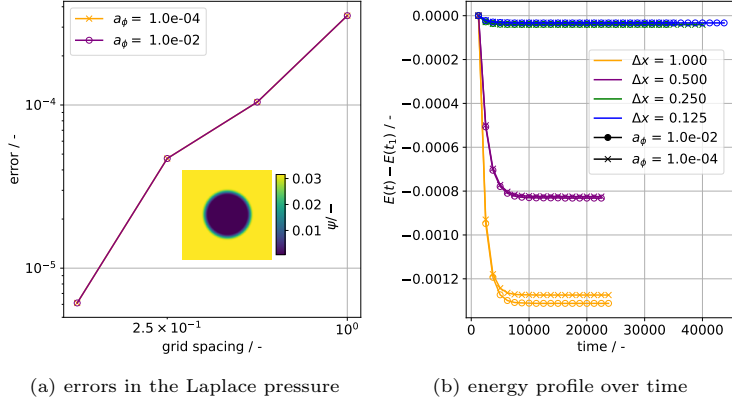


Figure 2: Results for the embedded phase case, showing non-uniform convergence to the sharp interface limit. The equilibrium grand potential ψ is shown exemplary as an inset; it clearly divides the two bulk phases with homogeneous values inside. The energy is observed to decrease monotonically.

For the triple junction geometry, a domain of size 192×96 is resolved at the coarsest scale with $\Delta x = 1$, with the long side being along the grain boundary to facilitate simulation of smaller dihedral angles at the same aspect ratio. The initial radius of the spherical phase on the grain boundary is 32. For simplicity the convergence study is limited to a single angle $\gamma_{\beta\beta} = 1, \gamma_{\alpha\beta} = 2 \rightarrow \theta \approx 151^\circ$, as results should be transferable to other angles except when approaching $\theta \rightarrow 0$ as complete dewetting is not captured by the model [3]. In addition, the coarsest resolution is also run with the FEuler integrator with a time step 0.9 times its stable time step. The remaining angles in the range 95° - 180° will use the practical resolution $\{\Delta x = 1, W = 2.5\}$ with $\gamma_{\alpha\beta} \in \{0.75, 1, 2, 6\}$.

Equilibrium is defined as a simple approximation to the measurement described in section 4.2. The positions of the 0.5 lines are determined on the horizontal and vertical lines passing through the center of the domain, using only a linear interpolation in the respective coordinate directions, with their respective differences giving approximations to L, S . This allows an estimate of the current dihedral angle θ , with equilibrium defined as a rate of change in angle by less than 1×10^{-11} rad over at least two diffusion times. The reported angle values are based on a more accurate marching squares reconstruction of the 0.5 contour lines of the phase α , which is only done after the simulation is completed.

The results of the grid convergence study are shown in fig. 3. Again, convergence to the sharp interface is observed with little influence from a_ϕ . At the coarsest resolution, a relative error of 1.4% is obtained. In this case, the energy does not decrease monotonically beyond the first output frame as shown in the inset of fig. 3(b); while there is a long-term decrease of energy, it is not monotonic. As is visible from the graph, on the scale of the energy reduction it is hardly noticeable without zooming closely to the data. Note that the FEuler integrator at the coarsest resolution also exhibits an non-monotonic behaviour as shown in the top inset. Rejection rates ranged from $< 1\%$ for $a_\phi = 1 \times 10^{-2}$

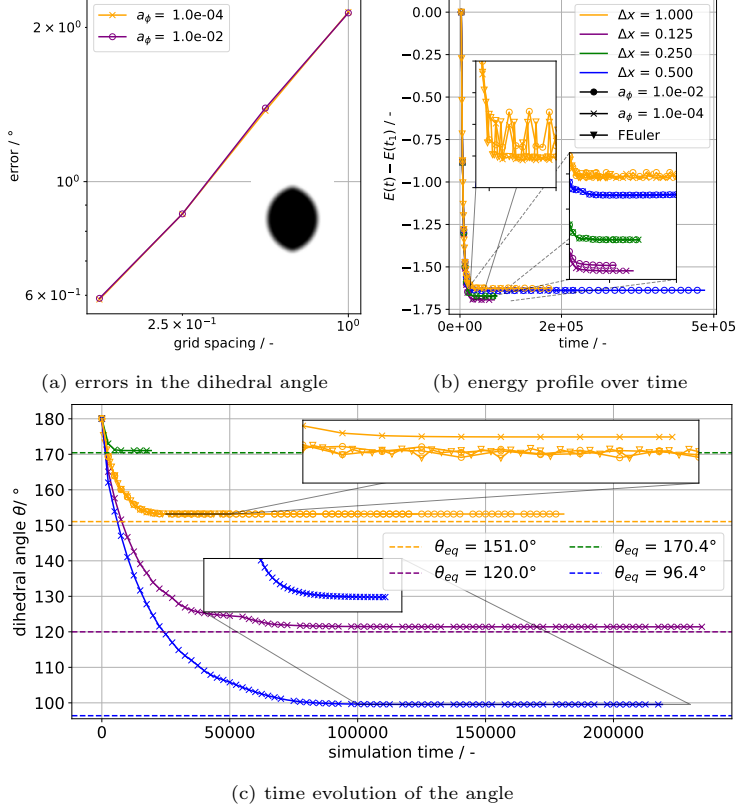


Figure 3: Results for the double triple junction case, showing convergence to the sharp interface but also non-monotonic decrease of energy; the equilibrium shape in the inset is that of the predicted vesica piscis shape. At the practical interface resolution, the analytical angle is still approximated well within the entire range of tested interface energy ratios. The circular marks in fig. 3(c) indicate STS2 results for $W = 3$ and the triangles for the FEuler integrator.

to up to 27% for $a_\phi = 1 \times 10^{-4}$. It is unlikely that step rejection is influenced by energy instability due to this split. We note though that energy instability was only apparent once the energy was almost converged; benchmarks not getting close to equilibrium are unlikely to probe energy stability properties of the integrator.

Results for all investigated angles are shown in fig. 3(c), with errors also on the order $O(1^\circ)$, with a tendency for the error to get larger at lower dihedral angles, as also observed by [3]. The insets show zooms on the evolution data, revealing that not necessarily a steady state is reached, but rather that the simulation may oscillate around one. The oscillations here are obtained for $W = 3$ (circles), i.e. the coarsest part of the grid convergence study, with either employed a_ϕ , but apparently not for $W = 2.5$, though both exhibited energy instability. Since energy instability does not strictly predict the oscillatory behaviour in the angle, it is hard to say whether these are related, but in any case the time integration error is small compared to the spatial error as evidenced by the close overlap for $W = 3$. Based on this, it seems that entering the energy instability regime has no practical influence on simulations approximating the

sharp interface equivalents.

5.2. Kinetic verification

Now that we know that the lack of strict energy stability does not significantly impact the equilibrium we can proceed to probe the kinetics of the integrators and get an impression of their performance. First is the embedded grain geometry described in section 4.3. We start again with a mesh convergence study to show that the proper limits are recovered, with a domain of size 512^2 being employed and an initial radius of $r = 220$ for the embedded grain, with the simulation being terminated upon reaching $t = 23 \times 10^3$ before the grain vanishes.

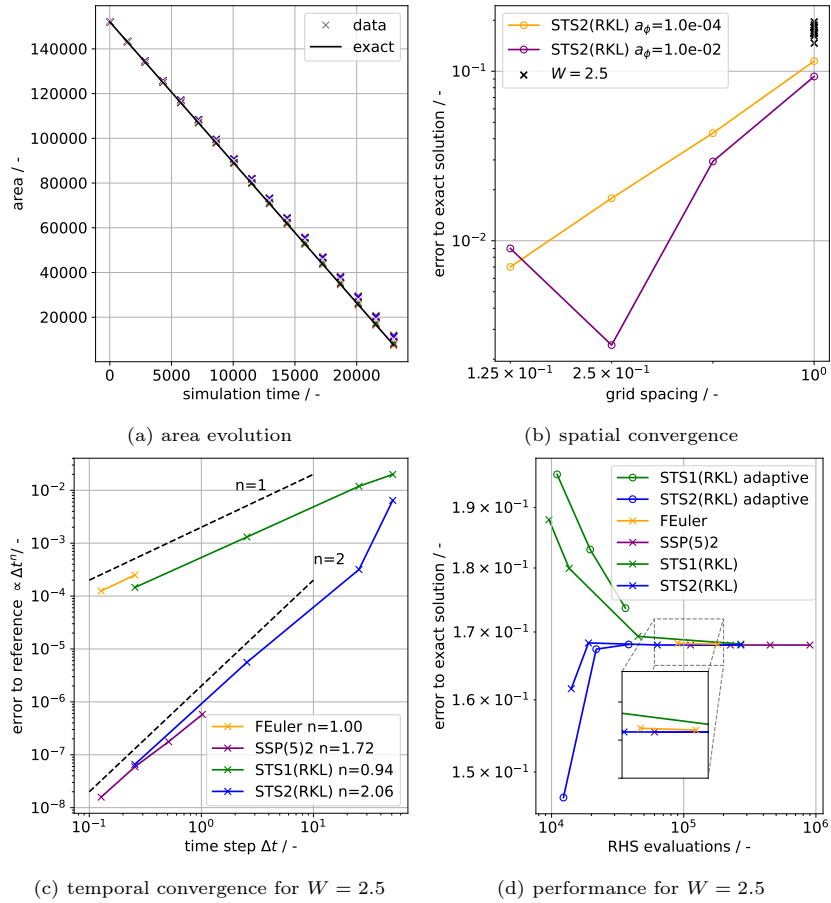


Figure 4: Results for the embedded grain geometry. The exact solution is closely approximated by all simulations. The convergence plot shows that for $a_\phi = 1 \times 10^{-2}$ the convergence stalls starting between $\Delta x = \{0.25, 0.125\}$, whereas consistent convergence is obtained for $a_\phi = 1 \times 10^{-4}$. Comparison to a reference solution shows the expected temporal orders. Comparing to the exact solution shows the STS integrators as the most efficient ones.

The results of this study and one using the integrators specified in Table 2 are shown in fig. 4. In fig. 4(a), we can observe that the qualitative time dependence of the exact solution is obtained by all simulations, but with quantitative differences. In fig. 4(b) convergence is observed throughout for time integration

tolerances of 1×10^{-4} , but for $a_\phi = 1 \times 10^{-2}$ this eventually limits the convergence. Interestingly, the error is smaller for the relaxed tolerance prior to this, suggesting that lower error may be achievable using a coarser tolerance due to cancellation of spatial and temporal errors. Thus for practical simulations, using a relatively coarse absolute tolerance can be beneficial for both speed and accuracy. Outside of the convergence part, the effect of time integration error is generally small as evidenced by the close clustering of crosses representing the remaining simulations. The largest of these, corresponding to a STS1 scheme with the largest timestep, has a relative error of about 3%, with most other simulations clustering around 2.7% relative error.

Next, looking at only the practical interface width results, we can compare the errors from fixed time step integrators to the reference integrator, which is shown in fig. 4(c). From this we can observe that generally the expected temporal error orders are obtained². The SSP(5)2 integrator tends to deviate from its order close to its stability limit. At larger time steps for the STS schemes, the interaction with the exact time matching output tends to force a mix of time steps which can affect the reported order. By instead comparing to the exact solution we can gauge which is the most efficient scheme: Plotting the error over the number of RHS evaluations as in fig. 4(d) we can observe that generally the STS schemes are the most efficient for this benchmark. The SSP(5)2 scheme at its stability limit is slightly more precise than the Euler scheme, but also requires slightly more function evaluations, and hence little is gained. Relative to the FEuler scheme the fixed STS schemes provide up to a factor of 9.4 speedup, whereas the adaptive ones are faster by a factor of 7-8, at little extra error or even smaller error at a slightly smaller speedup. Fixed timestepping for the STS schemes may outperform the adaptive one here, which is mainly due to a relatively large ratio of rejected steps (up to 29%). Note however that with fixed timestepping changing dynamics will not be adapted to, which can lead to inacceptably large errors.

The next case employs the Stefan problem as described in section 4.4. A one-dimensional domain of size 1800 is employed, with the left boundary held at the equilibrium concentration of $\beta, c_\beta = 0.98$, with the right one held at $c_\alpha = 0.2$. Together with the diffusivity $D = 1$ this results in a growth constant $A \approx 0.2412$ via eq. (50). The initial height of the β phase is 400. All results are collected in fig. 5(a) which shows a close match to the exact solution. We observe that the model converges upon grid refinement from fig. 5(b), with the practical resolution results still showing good accuracy. All results appear insensitive to the choice of a_ϕ ; informal variation of the remaining tolerances also showed little influence, suggesting the error is mainly controlled by diffuse interface effects, which naturally get scaled down due to the choice of $W(\Delta x)$. Considering that the rate of change of all field variables is much slower than in the previous case, the lack of sensitivity of the time integration error is quite sensible.

For the practical interface width the work-precision chart is shown in fig. 5(c). We observe, as would be suggested by previous results, that the obtained error is largely independent of the integrator and tolerance choice. Using either of the adaptive STS schemes here gives a speedup of about 4-5 with effectively no

²When used as ODE solvers for the Dahlquist test equation all obtain their order within a tolerance 5×10^{-2} .

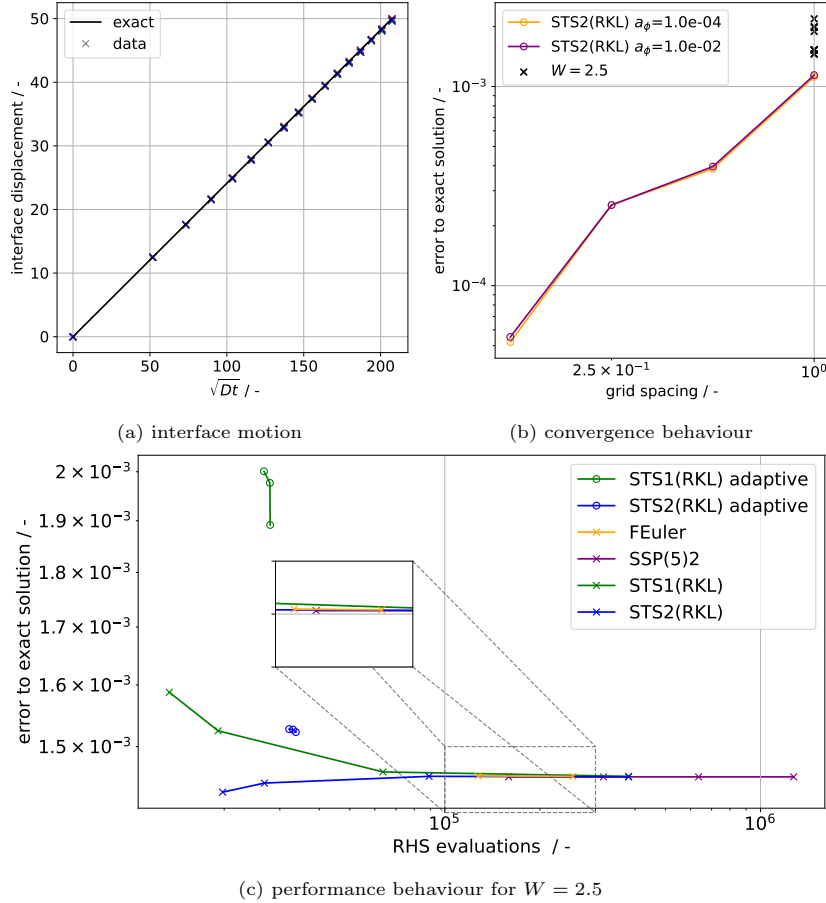


Figure 5: Results for the Stefan problem. The analytical solution is closely approximated and is being converged to with grid refinement. The choice of integrator seems to have little effect on the error and the STS integrators are observed to be the most efficient ones.

additional error; fixed timestepping produces speedups from 6 to 10. The phase-field tolerance seems to play little role for the performance here, suggesting that the temporal error is dominated by the concentration tolerance which was fixed for this study. Setting $a_c = a_\phi$ showed a performance improvement (up to a factor of 11) at no significant change in error.

Finally, none of the kinetic benchmarks showed any energy increase. It is likely that any actual energy error is drowned out by the magnitude of energy dissipation for these cases.

5.3. Grain growth with particles

The simulations are performed as described in section 4.5, yielding the grain size curves in fig. 6. For these, tolerances $a_\phi = 1 \times 10^{-2}$, $a_c = 1 \times 10^{-3}$ were chosen since early tests showed it had little influence as in the Stefan benchmark. An exponent close to $n = 2$ is observed for pure grain growth, whereas an increased exponent is observed for grain growth with mobile particles, as would be expected. Theoretically one would expect $n = 3$ for mass transport

through the vapor with the pore pressure being maintained at capillary equilibrium $p = \frac{2\gamma}{r}$ [30]. We suspect that this is due transient behaviour between the pure and pore-dragged behaviour, as the initial part of the curves are quite similar; reaching $n = 3$ likely requires significantly larger domains to allow for the dynamics to emerge. For the immobile particles we can compare the obtained limiting grain size (constant for about a time span of 200) to the prediction of Zener, which comes out to be $r_l \approx 0.27$. The simulation predicts a larger value of about 0.3, which is likely due to the interface width being of the same order of magnitude as the radius of curvature and overlap between particles effectively increasing the average radius. Hence we can say that even at quite coarse tolerances the STS schemes still recovers the essential features of the free-boundary problem we are concerned with.

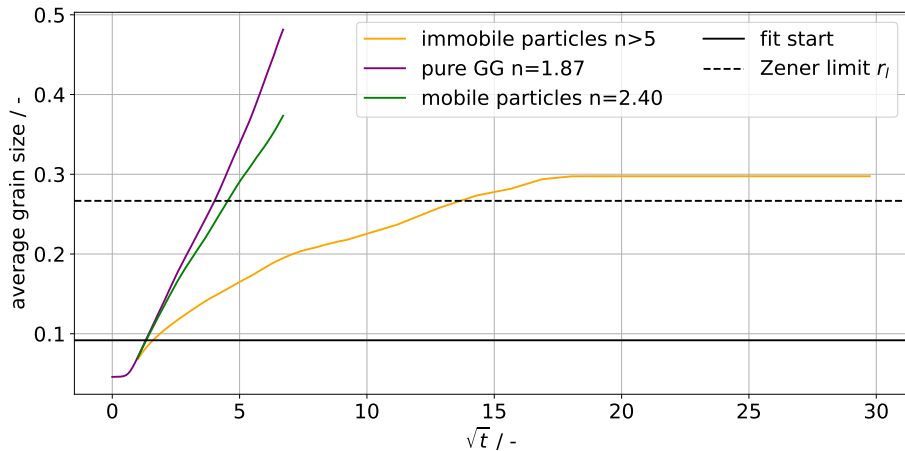


Figure 6: Results for grain growth, either pure, with immobile particles or mobile particles. The expected qualitative behaviour is observed, with exponents close to expectations being obtainable. For immobile particles, a limiting grain size is eventually reached.

Selected simulation snapshots are shown in fig. 7 with videos of the evolution deposited in the supplementary material. The immobile particle case is depicted with only the grain boundary (GB) network as the 0.5 isolevel of the $\phi_{gb} = \min(4 \sum_{i \neq \alpha, j \neq \alpha, j > i} \phi_j \phi_i, 1)$ field. The GBs are disturbed by circular holes due to the immobile particles and hence the particles' position may be inferred from these; note that the radius of the holes depends on both the particle radius and where the GB intersects them. Once a GB has accumulated sufficient particles, it apparently stops as highlighted; other faces of the grain may still advance however. The limiting grain size is reached once all GBs have a sufficient particle density.

The simulation with mobile particles show the triple lines (dark) defined as the 0.5 isolevel of the $\phi_{tj} = \min(27 \sum_{i,j > i,k > j} \phi_i \phi_j \phi_k, 1)$ field together with the 0.5 isolevel of the particle phase (bluish transparent). The pores co-move together with the grain boundaries and merge over time, reducing their number. As indicated by the closeup views, pores can attain a variety of shapes depending on their environment and time to equilibrate. If the pores only touch two grains, their shape tends to be a squashed sphere, though most pores touch more grains. In that case the shape is close to a rounded polyhedron with

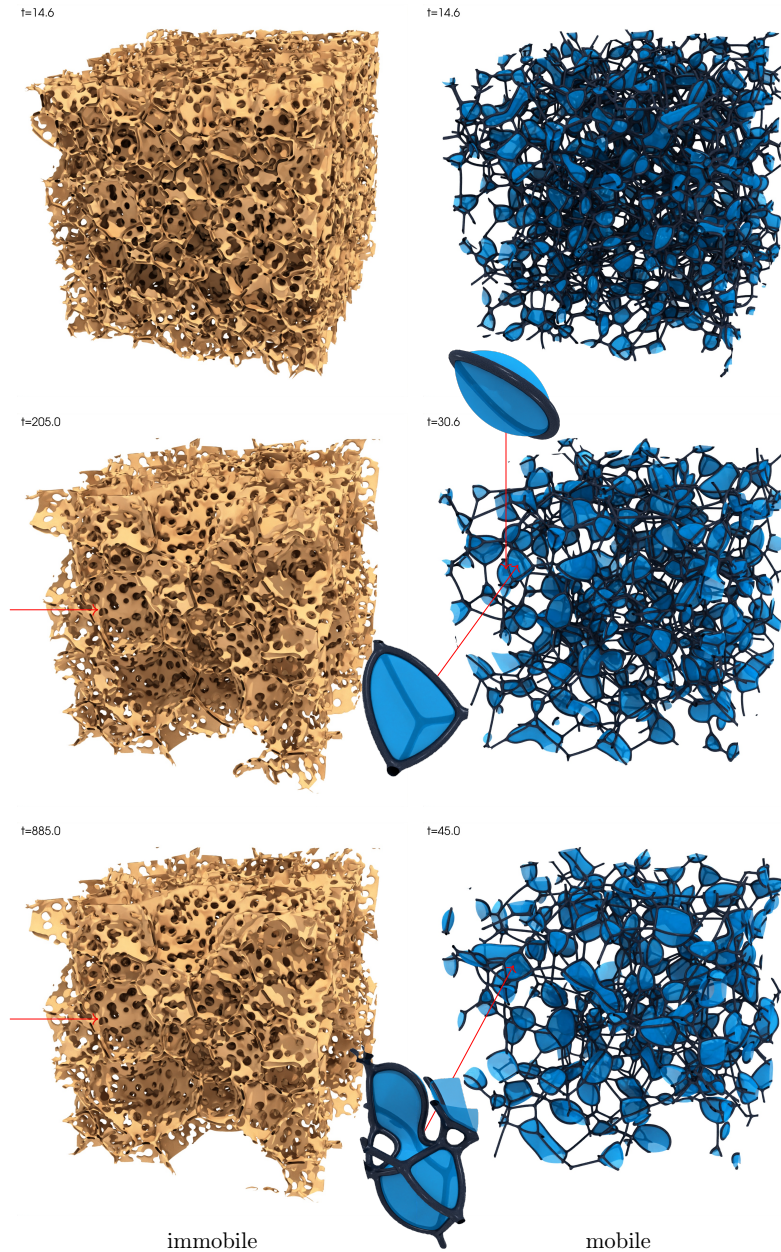


Figure 7: Selected snapshots of the 3D evolution with particles. For immobile particles (left column) GBs eventual stop their motion once they are sufficiently laden with particles as indicated. For mobile particles (pores) on the right column, these move and merge over time, allowing for continued, albeit slowed down, grain growth. Pores attain a variety of shapes depending on their surroundings and time to equilibrate.

vertices located at the enclosing grain triple lines in order to satisfy the surface tension balance; a tetrahedral example is shown for the middle row. This is in line with [33, 34], who employed a more regular geometry with pores being placed on quadruple points between a basal hexagonal polycrystal and one top crystal growing into this polycrystal. They observed that the pores took on shapes similar to ice-cream cones, with a triangular cross-section, which is the cross-section of a tetrahedron. Pores merging results in temporary irregular shapes as shown on the bottom. This pore is the result of the tetrahedral pore (four-sided face showing) from the middle row merging with the spheroidal pore shown in the middle panel and one nearby other tetrahedral pore. A video of the time evolution of this subdomain is deposited with the supplementary material. Due to the intentionally large pore mobility no pores are left behind within the growing grains.

The performance results are shown in Table 3. The RHS count for the FEuler integrator is estimated as $\frac{t_r}{\Delta t_e}$ as, like the table shows, the mobile pore case would be infeasible to compute with it³. The duration t_r is the end time minus any time offset, which for both particle-laden simulations is an offset of 1. For pure grain growth (GG), $\Delta t_e = 8.44 \times 10^{-4}$ is the stable Euler time step as the chemical driving force related terms vanish. For immobile particles this reduces to $\Delta t_e = 6.26 \times 10^{-5}$ via these terms. Finally, for mobile particles the stable step is $\Delta t_e = 2.82 \times 10^{-7}$ via the diffusion equation. For pure grain growth, the speedup is somewhat smaller as many phases dying off tends to force smaller time steps to accurately resolve the transition. However, once the problem becomes stiffer, this is more than compensated by the increased stability range of the integrator.

Table 3: 3D grain growth performance in terms of RHS evaluations

	pure GG	immobile particles	mobile particles
duration t_r	45	884	44
FEuler	53 279	14 110 453	156 288 000
STS2	14 288	1 224 604	1 365 954
speedup	3.73	11.5	114

6. Conclusion and outlook

Within the work it could be shown that energy stability has little influence on the error w.r.t. the sharp interface solution of two benchmark problems. Based on this, kinetic verifications showed behaviour convergent to sharp interface solutions, with practical choices of interface width still closely approximating these. Overall, both spatial and interfacial width related errors tended to dominate even at coarse integration tolerances; the phase-field could generally be integrated with absolute tolerances up to 1×10^{-2} without significant accuracy

³The STS2 simulation took about 16 hours on 4 NVIDIA A100 GPUs; the equivalent FEuler simulation would have taken about 80 days. Whether the system would have run uninterrupted for that long is another question.

loss at practical spatial resolution. With adaptive integrators, the temporal error only became visible after several levels of grid refinement. Speedups obtained range from a factor of 4 to 114 when using a STS integrator over the forward Euler integrator. This becomes the most pronounced when the equations exhibit multiple time scales, as is common in many manufacturing processes. The SSP(5)2 integrator — while integrating the time derivative more accurately — does not offer a speedup relative to the forward Euler integrator, as the spatial error dominates over the temporal error for practical resolutions. This likely extends to other “normal” explicit Runge-Kutta integrators as their stability domain scales linearly in the number of stages at best. As the STS integrator is not much more complicated than the forward Euler integrator to implement, there is little reason even for self-rolled codes not to prefer it over the forward Euler integrator.

If advective terms are included, the speedups would likely even be larger as accurate advection schemes such as WENO are relatively expensive to compute. By either using a splitting scheme or a partitioned scheme, these can be integrated to solve the evolution equations with the appropriate stability domains, while reducing the number of required number of advection term evaluations due to requiring fewer steps. The same idea applies to coupling to stationary problems e.g. stationary mechanics, which will need to be solved for far fewer times.

What bears further investigation is the relatively large number of step rejections for some benchmarks. This suggests that either the stability limit is passed or that some part (error estimator, time step adapter) in the step adaption machinery fails. The former might be probed by including a dynamical estimate of the largest eigenvalue of the system. If this doesn’t affect the rejection rate significantly, it might be that standard adapters need significant tuning in their coefficients to reduce their rejection rate as shown by [35] for compressible CFD problems.

A follow-up paper investigating both explicit and implicit schemes with a well potential is planned to complement the present limited investigation.

Author contributions

Marco Seiz: Conceptualization, Software, Methodology, Investigation, Data Curation, Validation, Visualization, Writing - original draft, Writing - review & editing. **Tomohiro Takaki:** Funding acquisition, Project administration, Resources, Writing - review & editing.

Conflicts of interest or competing interests

The authors declare that there are no conflicts of interest.

Data and code availability

The raw data is deposited with the supplementary material, except for the 3D simulation data for which only the processed data is deposited. It also contains electronic notebooks producing plots and auxiliary information. The 3D data may be shared upon reasonable request. The code required to reproduce the present work cannot be shared publicly.

Supplementary Material

The supplementary material of this paper is available at <https://zenodo.org/records/18320716>.

Acknowledgements

This paper is based on results obtained from a project, JPNP22005, commissioned by the New Energy and Industrial Technology Development Organization (NEDO).

References

- [1] M.N. Rahaman. *Ceramic Processing and Sintering*. CRC Press, Boca Raton, 2 edition, 2017.
- [2] Harald Garcke, Britta Nestler, and Barbara Stoth. A MultiPhase Field Concept: Numerical Simulations of Moving Phase Boundaries and Multiple Junctions. *SIAM J. Appl. Math.*, 60(1):295–315, January 1999.
- [3] Simon Daubner, Paul W. Hoffrogge, Martin Minar, and Britta Nestler. Triple junction benchmark for multiphase-field and multi-order parameter models. *Computational Materials Science*, 219:111995, February 2023.
- [4] Hector Gomez and Thomas J.R. Hughes. Provably unconditionally stable, second-order time-accurate, mixed variational methods for phase-field models. *Journal of Computational Physics*, 230(13):5310–5327, June 2011.
- [5] Andrew Christlieb, Jaylan Jones, Keith Promislow, Brian Wetton, and Mark Willoughby. High accuracy solutions to energy gradient flows from material science models. *Journal of Computational Physics*, 257:193–215, January 2014.
- [6] P. Vignal, N. Collier, L. Dalcin, D.L. Brown, and V.M. Calo. An energy-stable time-integrator for phase-field models. *Computer Methods in Applied Mechanics and Engineering*, 316:1179–1214, April 2017.
- [7] Jinchao Xu, Yukun Li, Shuonan Wu, and Arthur Bousquet. On the stability and accuracy of partially and fully implicit schemes for phase field modeling. *Computer Methods in Applied Mechanics and Engineering*, 345:826–853, March 2019.
- [8] Francisco Guillén-González and Giordano Tierra. Second order schemes and time-step adaptivity for Allen–Cahn and Cahn–Hilliard models. *Computers & Mathematics with Applications*, 68(8):821–846, October 2014.
- [9] Xinyu Cheng, Dong Li, Keith Promislow, and Brian Wetton. Asymptotic Behaviour of Time Stepping Methods for Phase Field Models. *J Sci Comput*, 86(3):32, March 2021.
- [10] M. A. Botchev, I. A. Fahurdinov, and E. B. Savenkov. Efficient and Stable Time Integration of Cahn–Hilliard Equations: Explicit, Implicit, and Explicit Iterative Schemes. *Comput. Math. and Math. Phys.*, 64(8):1726–1746, August 2024.

- [11] Seong Gyoong Kim, Won Tae Kim, and Toshio Suzuki. Phase-field model for binary alloys. *Physical Review E*, 60(6):7186–7197, December 1999.
- [12] I Steinbach and F Pezzolla. A generalized field method for multiphase transformations using interface fields. *Physica D: Nonlinear Phenomena*, 134:385–393, 1999.
- [13] Seong Gyoong Kim, Dong Ik Kim, Won Tae Kim, and Yong Bum Park. Computer simulations of two-dimensional and three-dimensional ideal grain growth. *Phys. Rev. E*, 74(6):061605, December 2006.
- [14] Cody J. Permann, Michael R. Tonks, Bradley Fromm, and Derek R. Gaston. Order parameter re-mapping algorithm for 3D phase field model of grain growth using FEM. *Computational Materials Science*, 115:18–25, April 2016.
- [15] Randall J. LeVeque. *Finite Difference Methods for Ordinary and Partial Differential Equations: Steady-State and Time-Dependent Problems*. Society for Industrial and Applied Mathematics, January 2007.
- [16] David I. Ketcheson. Highly Efficient Strong Stability-Preserving Runge–Kutta Methods with Low-Storage Implementations. *SIAM J. Sci. Comput.*, 30(4):2113–2136, January 2008.
- [17] Chad D. Meyer, Dinshaw S. Balsara, and Tariq D. Aslam. A second-order accurate Super TimeStepping formulation for anisotropic thermal conduction. *Monthly Notices of the Royal Astronomical Society*, 422(3):2102–2115, May 2012.
- [18] Chad D. Meyer, Dinshaw S. Balsara, and Tariq D. Aslam. A stabilized Runge–Kutta–Legendre method for explicit super-time-stepping of parabolic and mixed equations. *Journal of Computational Physics*, 257:594–626, January 2014.
- [19] Imre Fekete, Sidafa Conde, and John N. Shadid. Embedded pairs for optimal explicit strong stability preserving Runge–Kutta methods. *Journal of Computational and Applied Mathematics*, 412:114325, October 2022.
- [20] B.P. Sommeijer, L.F. Shampine, and J.G. Verwer. RKC: An explicit solver for parabolic PDEs. *Journal of Computational and Applied Mathematics*, 88(2):315–326, March 1998.
- [21] Gustaf Söderlind and Lina Wang. Adaptive time-stepping and computational stability. *Journal of Computational and Applied Mathematics*, 185(2):225–243, January 2006.
- [22] Sanjiv Shanmugavelu, Mathieu Taillefumier, Christopher Culver, Oscar Hernandez, Mark Coletti, and Ada Sedova. Impacts of floating-point non-associativity on reproducibility for HPC and deep learning applications. In *SC24-W: Workshops of the International Conference for High Performance Computing, Networking, Storage and Analysis*, pages 170–179, Atlanta, GA, USA, November 2024. IEEE.

- [23] Hector Gomez and Kristoffer G. Van Der Zee. Computational Phase-Field Modeling. In *Encyclopedia of Computational Mechanics Second Edition*. Wiley, December 2017.
- [24] J. R. Bradley and H. I. Aaronson. The stereology of grain boundary allotriomorphs. *Metall Trans A*, 8(2):317–322, February 1977.
- [25] Robert W. Balluffi, Samuel M. Allen, and W. Craig Carter. *Kinetics of Materials*. Wiley, 2005.
- [26] Abhik Choudhury and Britta Nestler. Grand-potential formulation for multicomponent phase transformations combined with thin-interface asymptotics of the double-obstacle potential. *Physical Review E - Statistical, Nonlinear, and Soft Matter Physics*, 85(2), 2012.
- [27] Y Liu and B R Patterson. Determination of pore mobility during sintering. *Metall Mater Trans A*, 25:81–87, 1994.
- [28] A Harun, E Holm, M Clode, and M Miodownik. On computer simulation methods to model Zener pinning. *Acta Materialia*, 54(12):3261–3273, July 2006.
- [29] V. Rehn, J. Hötzer, W. Rheinheimer, M. Seiz, C. Serr, and B. Nestler. Phase-field study of grain growth in porous polycrystals. *Acta Materialia*, 174:439–449, 2019.
- [30] F. A. Nichols. Theory of Grain Growth in Porous Compacts. *Journal of Applied Physics*, 37(13):4599–4602, December 1966.
- [31] H Riedel and J Svoboda. A THEORETICAL STUDY OF GRAIN GROWTH IN POROUS SOLIDS DURING SINTERING. *Acta metall. mater.*, 41(6):1929–1936, 1993.
- [32] Mark Miodownik, Elizabeth A. Holm, and Gregory N. Hassold. Highly parallel computer simulations of particle pinning: Zener vindicated. *Scripta Materialia*, 42(12):1173–1177, June 2000.
- [33] Veena Tikare, Mark A. Miodownik, and Elizabeth A. Holm. Three-Dimensional Simulation of Grain Growth in the Presence of Mobile Pores. *Journal of the American Ceramic Society*, 84(6):1379–1385, June 2001.
- [34] Johannes HÖTZER, Veronika REHN, Wolfgang RHEINHEIMER, Michael J. HOFFMANN, and Britta NESTLER. Phase-field study of pore-grain boundary interaction. *Journal of the Ceramic Society of Japan*, 124(4):329–339, 2016.
- [35] Hendrik Ranocha, Lisandro Dalcin, Matteo Parsani, and David I. Ketcheson. Optimized Runge-Kutta Methods with Automatic Step Size Control for Compressible Computational Fluid Dynamics. *Commun. Appl. Math. Comput.*, 4(4):1191–1228, December 2022.